Catalysis on singly dispersed bimetallic sites

Shiran Zhang[1,2,*], Luan Nguyen[1,2,*], Jin-Xia Liang[3,4,*], Junjun Shan[1,2], Jingyue (Jimmy) Liu[5], Anatoly I. Frenkel[6], Anitha Patlolla[6], Weixin Huang[1,2], Jun Li[3] & Franklin (Feng) Tao[1,2]

A catalytic site typically consists of one or more atoms of a catalyst surface that arrange into a configuration offering a specific electronic structure for adsorbing or dissociating reactant molecules. The catalytic activity of adjacent bimetallic sites of metallic nanoparticles has been studied previously. An isolated bimetallic site supported on a non-metallic surface could exhibit a distinctly different catalytic performance owing to the cationic state of the singly dispersed bimetallic site and the minimized choices of binding configurations of a reactant molecule compared with continuously packed bimetallic sites. Here we report that isolated Rh_1Co_3 bimetallic sites exhibit a distinctly different catalytic performance in reduction of nitric oxide with carbon monoxide at low temperature, resulting from strong adsorption of two nitric oxide molecules and a nitrous oxide intermediate on Rh_1Co_3 sites and following a low-barrier pathway dissociation to dinitrogen and an oxygen atom. This observation suggests a method to develop catalysts with high selectivity.

[1] Department of Chemical and Petroleum Engineering, University of Kansas, Lawrence, Kansas 66047, USA. [2] Department of Chemistry, University of Kansas, Lawrence, Kansas 66047, USA. [3] Department of Chemistry and Key Laboratory of Organic Optoelectronics and Molecular Engineering of Ministry of Education, Tsinghua University, Beijing 100084, China. [4] Guizhou Provincial Key Laboratory of Computational Nano-Material Science, Guizhou Normal College, Guiyang 550018, China. [5] Department of Physics, Arizona State University, Tempe, Arizona 85287, USA. [6] Department of Physics, Yeshiva University, New York, New York 10016, USA. * These authors contributed equally to this work. Correspondence and requests for materials should be addressed to J.L. (email: junli@tsinghua.edu.cn) or to F.T. (email: franklin.feng@ku.edu).

A single reaction event of heterogeneous catalysis occurs on a specific catalytic site at atomic or nanoscale[1–3]. An active catalytic site catalyses a reaction by decreasing its activation barrier through a reaction pathway different from that without a catalyst. Typically, a catalytic site may consist of one, two or a few atoms of surface of a catalyst particle. Atoms of a catalytic site arrange into a configuration that essentially offers a specific electronic structure for the catalytic cycle. Bimetallic nanoparticle catalysts play significant roles in chemical and energy transformations since the second metal (A) could tune catalytic performance of a monometallic catalyst (M) through ligand effect, geometric effect, bi-functional effect or lattice strain effect[2–5] (Fig. 1a,b). Atoms of a catalytic site of a bimetallic nanoparticle could come from more than one element (for example, M and A in Fig. 1c). Alternatively, they could come from the same element (for example, M in Fig. 1d) though surface of the bimetallic nanoparticles has both elements M and A. In the latter case, atoms of element A are the modifier of electronic structure but do not directly participate into the catalysis. When metal atoms of a catalytic site come from two different metal elements such as M and A, we term it a 'bimetallic' site (Fig. 1c); in this case, atoms from both M and A directly participate into the catalytic reaction. One type of such bimetallic sites is referred to M_1A_n (M and A: metal elements, $n \geq 1$), in which both M and A directly participate into a catalytic reaction. The feature of such a bimetallic site is that there is only one atom of M though there is one or more atoms of A.

Typically, such a bimetallic site, M_1A_n is continuously packed on surface of a bimetallic nanoparticle. Thus, the M_1A_n sites on surface of a bimetallic nanoparticle are at a metallic state. However, if such bimetallic sites (M_1A_n) are separately anchored on the surface of a non-metallic support such as a transition metal oxide, these isolated bimetallic sites (Fig. 1f) are at cationic state. Such isolated bimetallic sites could provide a different surface process including adsorption and dissociation for a reactant molecule or/and an intermediate compared with continuously packed bimetallic sites on a bimetallic nanoparticle. Such a different surface process could facilitate dissociation of a reactant molecule and then accelerate a subsequent coupling with another reactant molecule/dissociated species to form an intermediate or a product molecule. In addition, the single dispersion of atom M of an isolated bimetallic site (M_1A_n) minimizes choices of potential binding configurations of a reactant molecule, dissociated species, or intermediate on catalyst surface (Fig. 1f), in contrast to the potential multiple choices of binding configurations such as on-top, bridge or hollow sites on the surface of a bimetallic nanoparticle. For example, on an M–A bimetallic nanoparticle surface, a R_2 molecule could bind to atop, bridge or even hollow site of M atoms. However, R_2 can bind to M atom through only an atop binding (Fig. 1f) on an isolated bimetallic site M_1A_n. Consequently, the minimized choices of binding configurations of reactant, dissociated species or intermediate on isolated M_1A_n sites may enhance catalytic selectivity by following a specific reaction pathway if there are multiple pathways on a bimetallic nanoparticle.

Here we report the preparation of a catalyst consisting of singly dispersed bimetallic sites (SBMS) Rh_1Co_3 through controlled oxidation and reduction processes with the aid of *in situ* track of evolution of chemistry and structure of the catalyst precursor, and the unique catalytic performance of Rh_1Co_3 in terms of 100% selectivity for reducing NO to N_2 at 110 °C with a much higher activity than Rh–Co bimetallic nanoparticles at this temperature. Our results illustrate that isolation of bimetallic sites of bimetallic nanoparticles could be used to develop catalysts with higher selectivity or activity.

Results

Synthesis of a catalyst of isolated bimetallic sites Rh_1Co_3. As shown in Fig. 2, the synthesis of a catalyst of isolated bimetallic sites begins with the formation of hydroxide species $M(OH)_z$ on the surface of a reducible oxide A_xO_y, followed by a calcination at 150 °C in O_2 to anchor M to the surface through formation of M–O–A bonds between singly dispersed $M(OH)_z$ species and the surface of the support A_xO_y, and concluded with a controlled reduction at 300 °C in 5% H_2 to remove some of the oxygen atoms bonded to both atom M_1 and atoms A of the surface, thus forming M–A bonds on the surface of the oxide (Fig. 2).

An over-reduction of the support A_xO_y typically forms an ultrathin bimetallic film of metals M and A; in this case, the guest metal atoms M may alloy with metal atoms of A to form a bimetallic thin layers (Supplementary Fig. 1) instead of isolated M_1A_n bimetallic sites. On the other hand, a less reduction in terms of a reduction at a relatively low temperature could not remove oxygen atoms between M_1 and A of M_1O_n/A_xO_y; in this
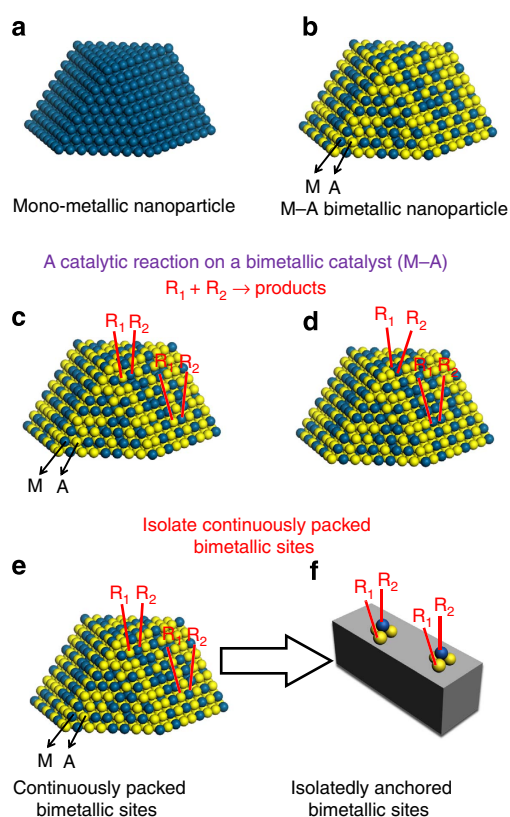
Figure 1 | Schematic illustration of the isolation of continuous bimetallic sites of alloy nanoparticle to SBMS. Blue and yellow balls represent atoms of metal elements M and A. R_1 and R_2 are different reactants. (**a**) Schematic of a monometallic nanoparticle. (**b**) Schematic of a bimetallic nanoparticle. (**c**) Surface of an M-A bimetallic nanoparticle consisting of continuous bimetallic sites; R_1 and R_2 bind to A and M atoms, respectively. (**d**) Surface of an M-A bimetallic nanoparticle consisting of continuous bimetallic sites; however, R_1 and R_2 only bind to atoms of metal M instead of A; A is only the modifier of electronic or/and geometric structure. (**e**) Surface of an M-A bimetallic nanoparticle consisting of continuous bimetallic sites. (**f**) Isolated bimetallic sites anchored on a non-metallic support; different from the multiple binding configurations of R_2 on an M-A bimetallic nanoparticle, here R_2 can only bind to the single atom M through an on-top binding configuration.
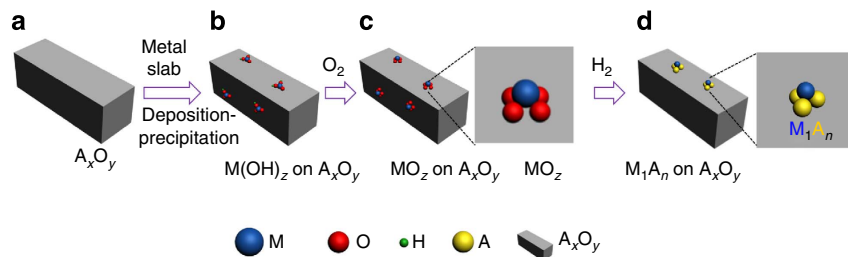
Figure 2 | Schematic of synthesis of a catalyst of singly dispersed bimetallic sites M_1A_n. (**a**) Well-crystallized reducible oxide substrate, A_xO_y. (**b**) Deposition of hydroxide species of guest metal, $M(OH)_z$, to surface of the oxide support, A_xO_y; a low concentration of M cations (0.5 wt% or less) allows them to be singly dispersed on the surface of A_xO_y; the atomic ratio of M atoms to A atoms of the topmost layer of atoms A of A_xO_y is typically <5–10%; $M(OH)_z$ species are weakly bound to the surface of A_xO_y. (**c**) Formation of singly dispersed M_1O_n species upon oxidation in 5% O_2 at 150 °C; M cations are bonded to A_xO_y surface through M–O–A bonds. (**d**) A controlled reduction in 5% H_2; removal of oxygen atoms between M and A atoms by reduction in H_2 makes M directly bond with A atoms of oxide support, forming an M_1A_n site; as M atoms are singly dispersed on A_xO_y (due to the low concentration of guest atoms M), the formed M_1A_n bimetallic sites are isolated. They are called singly dispersed bimetallic sites.
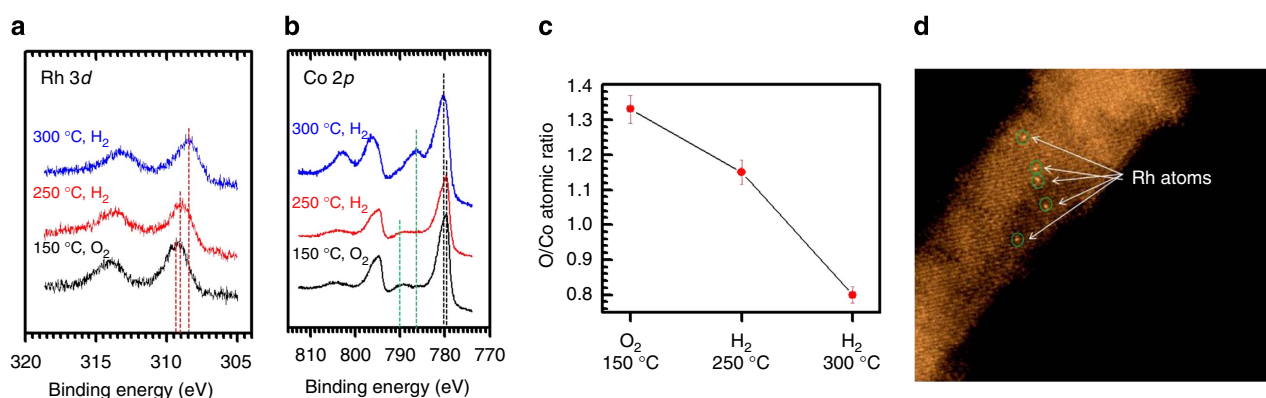
Figure 3 | In situ studies of surface chemistry. *In situ* studies of surface chemistry of the catalyst precursor in the preparation of the catalysts of singly dispersed Rh_1Co_3 bimetallic sites with ambient pressure XPS. (**a**) Rh 3d photoemission features during oxidation and reduction processes as marked. (**b**) Co 2p photoemission features during oxidation and reduction. (**c**) Evolution of O/Co atomic ratio under different reaction conditions; the error bar is ±5% of the measured data. (**d**) HAADF-STEM image (14 × 11 nm) of Rh_1Co_3/CoO prepared with oxidation at 150 °C in 5% O_2 and reduction at 300 °C in 5% H_2; the bright spots are Rh atoms of Rh_1Co_3 catalytic sites; Rh_1Co_3 sites are singly dispersed.

case, the guest metal atom M still bonds to the surface oxygen atoms instead of the surface metal atom(s) A; thus, no bimetallic M_1A_n site is formed. Therefore, an appropriate reduction of the catalyst precursor M_1O_n/A_xO_y is crucial for the preparation of a catalyst of isolated M_1A_n bimetallic sites, M_1A_n/A_xO_y.

Co_3O_4 was chosen as one example of oxide support (A_xO_y). It generates oxygen vacancies on its surface readily when reduced in a reducing environment[6,7]. Reduction of nitric oxide with CO was used as a probing reaction. Co_3O_4 nanorods were synthesized through a colloidal method[8–10]. Rh atoms were introduced to the surface of Co_3O_4 nanorods through precipitation of Rh^{3+} in the format of $Rh(OH)_z$ species (Fig. 2b). $Rh(OH)_z$ weakly binds to the surface of Co_3O_4. Evolution of chemical environment of Rh atoms and the surface of cobalt oxide during appropriate oxidation and reduction steps was tracked with an *in situ* ambient pressure X-ray photoelectron spectroscopy (AP-XPS)[11]. For all *in situ* studies of this work, data were collected while gaseous reactants remained around a catalyst at a certain temperature.

During oxidation in O_2, Rh atoms are at a cationic state with a high binding energy of Rh $3d_{5/2}$ at 309.4 eV (Fig. 3a)[12]. Upon the formation of Rh_1O_n species on Co_3O_4 at 150 °C in O_2, reductions in H_2 at different temperatures were performed. In the reduction at 250 °C in 5% H_2, Rh 3d down-shifted by 0.4 to 309.0 eV (Fig. 3a). After the reduction in 5% H_2 at 250 °C, a following reduction in H_2 at 300 °C was performed to form isolated

bimetallic sites of Rh_1Co_3, as is schematically shown in Fig. 2d. During the reduction at 300 °C, Rh $3d_{5/2}$ further down-shifted by 0.5 eV to 308.5 eV (Fig. 3a). Down-shift of binding energy from 309.4 to 308.5 eV clearly suggests a change of the binding environment of Rh atoms during the reduction. The down-shift to 308.5 eV instead of 307.4 eV of metallic Rh shows that Rh atoms of the catalyst upon a reduction at 300 °C in 5% H_2 are not at a metallic state. Figure 4d is the image of HAADF (high-angle annular dark-field) through STEM (scanning transmission electron microscopy) of Rh_1Co_3/CoO after catalysis at 400 °C, in which singly dispersed Rh atoms appear as separated spots with high contrast due to the larger atomic number of Rh atoms in contrast to Co (ref. 13). This is consistent with the single dispersion of Rh atoms of catalysts after catalysis at 400 °C confirmed with *in situ* EXAFS (Fig. 4a).

In situ EXAFS technique was used to track the evolution of the coordination environment of Rh atoms of the catalyst precursor along the reaction at 150 °C in 5% O_2, at 300 °C in 5% H_2 and at 400 °C in the mixture of NO and CO (Fig. 4a, Table 1 and Supplementary Fig. 2). The fitted structural parameters of Co and O atoms coordinating to Rh atoms of catalyst particles being annealed at 150 °C in O_2 show that (1) Rh atoms of the catalyst precursor are singly dispersed and (2) these Rh atoms on the cobalt oxide only bond with oxygen atoms with a coordination number of ~4–5 (Table 1). EXAFS study performed on the catalyst upon reduction in 5% H_2 at 300 °C shows that Rh atoms
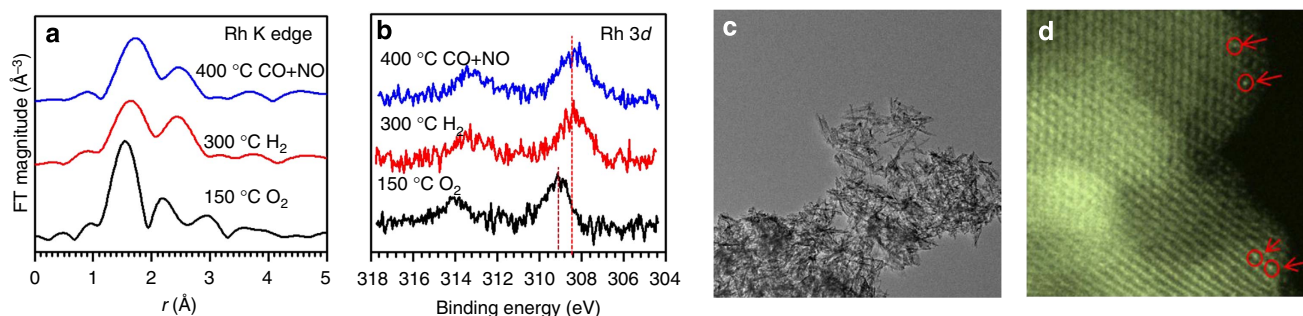
Figure 4 | Characterizations in the preparation of isolated bimetallic sites. Characterizations in the preparation of isolated bimetallic sites Rh_1Co_3/CoO and during catalysis by *in situ* EXAFS, *in situ* AP-XPS, and *ex situ* HAADF-STEM. (**a**) *r*-Space spectra of Rh K edge of catalyst precursor at 150 °C in O_2 (black line), a following reduction at 300 °C in H_2 (red line) and during catalysis at 400 °C from *in situ* EXAFS studies (blue line). (**b**) Photoemission feature of Rh 3*d* of catalyst precursor at 150 °C in O_2 (black line), a following reduction at 300 °C in H_2 (red line) and during catalysis at 400 °C (blue line) from *in situ* AP-XPS studies. (**c**) TEM image (700 × 700 nm) of Rh_1Co_3/CoO after catalysis. (**d**) HAADF-STEM image of the catalyst of isolated Rh_1Co_3 bimetallic sites after catalysis at 400 °C; the red arrows mark the Rh atoms that are singly dispersed on CoO.

Table 1 | Coordination numbers and bond lengths.

Reaction temperature	Reactants	Measurement condition	N(Rh–O)	N(Rh–Co)	N(Rh–Rh)	R(Rh–O) (Å)	R(Rh–Co) (Å)
150 °C	O_2	25 °C, O_2	4.5 ± 0.6	0.3 ± 0.4	0	2.033 ± 0.008	2.55 ± 0.03
300 °C	H_2	25 °C, CO + NO	2.6 ± 1.0	1.8 ± 0.9	0	2.13 ± 0.04	2.61 ± 0.02
400 °C	CO + NO	25 °C, CO + NO	1.7 ± 0.5	1.3 ± 0.7	0	2.15 ± 0.03	2.60 ± 0.02

Coordination number of O, Co and Rh atoms around a Rh atom and bond lengths of Rh–O and Rh–Co based on EXAFS studies of precursor of Rh_1Co_3/CoO catalyst at 150 °C in 5% O_2, 300 °C in 5% H_2 and of catalyst of Rh_1Co_3/CoO during catalysis at 400 °C in a mixture of 5% CO + 5% NO.

still preserve their single dispersion [CN(Rh–Rh) = 0)] and bond with cobalt and oxygen atoms, [CN(Co–Rh) = 2.6 and CN(O–Rh) = 1.8]. The direct bonding of Rh to Co (Table 1) shows the formation of Rh–Co bonds. Since a Rh atom is isolated from other Rh atoms and bonds with Co atoms, we term the ensemble Rh_1Co_n a singly dispersed bimetallic site or an isolated bimetallic site (Fig. 2d). The average coordination number of Co atoms directly bonded to a Rh atom is almost 2 based on EXAFS studies. For simplicity and consistence with the Rh_1Co_3 structure on CoO proposed through optimization in the following computational studies, Rh_1Co_3/CoO is used as the term of this type of isolated bimetallic sites in this communication.

It is noted that an over-reduction in 5% H_2 at a relatively high temperature of 400 °C forms metallic Co surface layers consisting of a small amount of Rh atoms, as is evidenced by the low binding energy of Co $2p_{3/2}$ at 778.3 eV and Rh $3d_{5/2}$ at 307.2 eV (Supplementary Fig. 1). However, AP-XPS studies show that a reduction in 5% H_2 at 250 °C does not form a Rh–Co bond since Rh $3d_{5/2}$ is still ~309.0 eV instead of 308.5 eV (Fig. 3). Thus, an appropriate reduction temperature is the key for the formation of singly dispersed Rh_1Co_3 bimetallic sites.

Other than the evolution of coordination environment of Rh atoms in the preparation of a catalyst, one obvious change of the support, Co_3O_4 during reduction at 300 °C in 5% H_2 is the formation of cobalt monoxide in the surface region, evidenced by the observed new peak of Co $2p_{3/2}$ at 786.4 eV (Fig. 3b). This peak is attributed to the characteristic satellite peak of Co $2p_{3/2}$ of Co^{2+} in an octahedral coordination with oxygen atoms in CoO at 786.4 eV (refs 14,15). Thus, by referring to the characteristic satellite peak of Co $2p_{3/2}$ of CoO reported in literature[14,15], the photoemission feature of Co $2p_{3/2}$ collected at 300 °C in 5% H_2 is assigned to CoO. In addition, the formation of CoO is also supported by the O/Co atomic ratio of the catalyst experiencing a

reduction at 300 °C in 5% H_2, 0.80 (Fig. 3c), which was measured by taking the stoichiometric ratio of Co_3O_4, 1.33 at room temperature as a reference to calibrate the measured atomic ratios (O/Co).

As shown in Supplementary Table 1, the theoretical atomic ratio of all Rh atoms to all Co atoms of the topmost layer of Co atoms of CoO nanoparticles is 1.40%. The measured ratios of the catalyst during catalysis at 150 °C and 400 °C are 1.26 and 1.25%, respectively (Supplementary Table 1), which are quite close to the calculated ideal value, 1.40% (Supplementary Methods). These studies suggest that Rh atoms are mainly located on the topmost surface of catalyst particles without obvious thermal diffusion to deep layers. More information on the calculation of these atomic ratios of Rh to Co can be found in Supplementary Methods and Supplementary Figs 11–14.

Catalytic performances of isolated and continuous bimetallic sites. After the oxidation of the catalyst precursor in 5% O_2 at 150 °C with a following reduction at 300 °C in 5% H_2, the catalyst was cooled to 80 °C in 5% H_2. Once the 5% H_2 was purged, 30 ml min^{-1} 10% CO (balanced with Ar), 20 ml min^{-1} 5% NO (balanced with Ar) and 10 ml min^{-1} 99.999% Ar were mixed and then introduced. Measurements of catalytic performance on the catalyst of isolated Rh_1Co_3 sites anchored on CoO, Rh_1Co_3/CoO were performed in a fixed-bed flow reactor. N_2O is the by-product of this reaction. Rh_1Co_3/CoO exhibits a catalytic selectivity of 100% for the production of N_2 at a temperature as low as 110 °C (Fig. 5a).

Rh–Co bimetallic nanoparticles supported on SiO_2, Rh–Co bimetallic nanoparticles supported on CoO and a pure CoO catalyst were prepared with the details described in the section of method. The formation of Rh–Co alloy NP supported on CoO was confirmed with TEM (Supplementary Fig. 3) and XRD (Supplementary Fig. 4). Rh–Co bimetallic nanoparticle supported
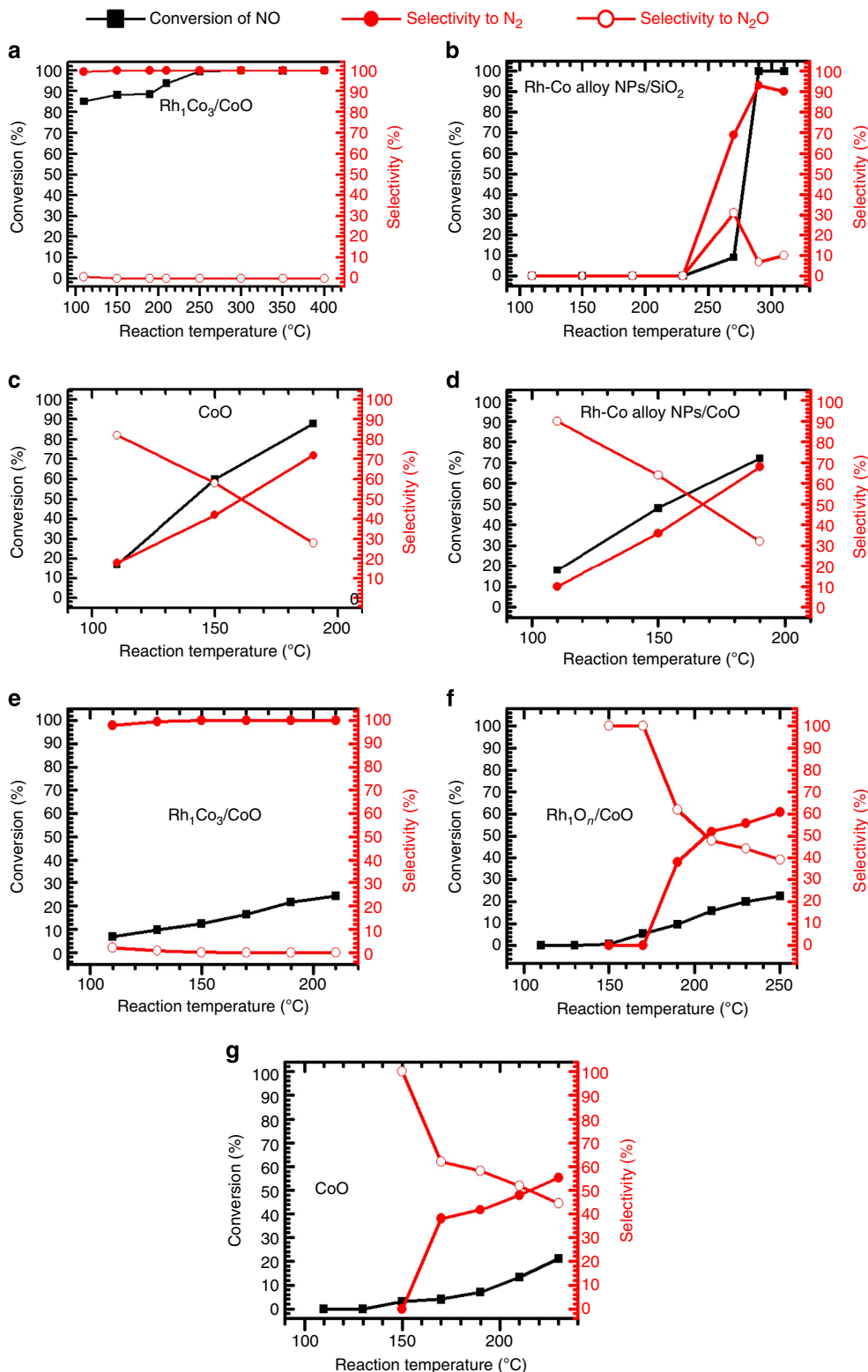
Figure 5 | Catalytic performances of catalysts measured under different conditions. (**a**) Rh_1Co_3/CoO, (**b**) Rh–Co alloy nanoparticles (2.5 nm) supported on SiO_2, (**c**) pure CoO and (**d**) Rh–Co bimetallic nanoparticles supported on CoO. Catalytic activity and selectivity of these catalysts (**a–d**) were measured with the exactly same condition: mixture of 20 ml min^{-1} 15% NO balanced with Ar, 30 ml min^{-1} 10% CO and 10 ml min^{-1} 99.999% Ar; 10 mg of a catalyst was used in each catalytic measurement. (**e–g**) Catalytic performance 5 mg of Rh_1Co_3/CoO, 5 mg of Rh_1O_n/CoO and 10 mg of CoO at kinetic controlled region (conversion is lower than 20%); for these measurements in kinetics-controlled regime, 80 ml 15% NO (balanced with Ar) and 12 ml pure CO were mixed and introduced into the reactor.

on SiO_2 is not active at any temperatures <250 °C (Fig. 5b). In addition, the activity and selectivity for the production of N_2 on Rh–Co bimetallic nanoparticles supported on CoO at 110 °C are

only 20% and 10%, respectively (Fig. 5d). Compared with Rh–Co bimetallic nanoparticles supported on CoO, obviously the isolated bimetallic sites Rh_1Co_3 supported on CoO exhibit an outstanding

catalytic performance in terms of high catalytic activity and 100% selectivity for production of N_2 at a temperature as low as 110 °C (Fig. 5a). Supplementary Table 2 lists catalytic performances at 110 °C measured under kinetics controlled regime (Fig. 5e–g). Clearly, isolated Rh_1Co_3 bimetallic sites anchored on CoO (Rh_1Co_3/CoO) exhibit a much higher activity than Rh–Co bimetallic nanoparticles supported on SiO_2, pure CoO and Rh–Co bimetallic nanoparticles supported on CoO. It is noted that Rh nanoparticles[16] or Rh-based bimetallic nanoparticles[17–20] and Rh single crystals[21] are not active at a temperature < 240 °C; selectivities for the production of N_2 on Rh nanoparticles at 240 °C (ref. 16) and Rh(100) at 255 °C (ref. 21) are only ~30% and ~25%, respectively. Overall, the isolated bimetallic sites Rh_1Co_3 of Rh_1Co_3/CoO exhibit an outstanding catalytic performance in terms of quite high catalytic activity and 100% selectivity for the reduction of NO to N_2 at a temperature as low as 110 °C.

In situ AP-XPS studies of the catalyst during catalysis at a temperature up to 400 °C showed that Rh atoms of Rh_1Co_3/CoO catalyst remains at its oxidizing state (Fig. 4b). The high binding energy of Rh $3d$ of isolated Rh_1Co_3 sites anchored on CoO, 308.5 eV, suggests the cationic nature of the Rh atoms in isolated bimetallic sites during catalysis at 400 °C. The preservation of single dispersion of the Rh atoms and the coordination of Co to Rh were supported by *in situ* studies of EXAFS during catalysis (Fig. 4a and Table 1) and *ex situ* studies of the catalyst after catalysis at 400 °C using HAADF-STEM (Fig. 4d). These characterizations suggest that the isolated bimetallic sites are preserved during catalysis and responsible for the high activity and 100% selectivity for N_2 production. In addition, catalytic performances of Rh_1Co_3/CoO and pure CoO under kinetics-controlled regions were measured (Fig. 5e,g). By using the number of Rh atoms as the number of Rh_1Co_3 sites, turnover frequencies (TOFs) of the production of N_2 were calculated and listed in Supplementary Table 2. The turnover frequency of Rh_1Co_3/CoO at 110 °C is 4.4 N_2 molecules per bimetallic site per second.

To confirm the importance of direct bonding of Co atoms to a Rh atom in Rh_1Co_3/CoO, catalyst Rh_1O_n/CoO was synthesized with the method described in the Methods section. A two-step method was used in the preparation of Rh_1O_n/CoO. CoO substrate was prepared by annealing Co_3O_4 to 300 °C in 5% H_2; the phase transformation was confirmed with XRD; in the second step Rh cations are loaded to the surface of CoO through deposition–precipitation with a following calcination in H_2 at 200 °C for 1 h; the adsorbed $Rh(OH)_z$ species were transferred to Rh_1O_n. The existence of Rh atoms on the surface was supported with the preservation of Rh/Co ratio (all Rh atoms to all Co atoms of the topmost layer of Co of CoO) measured with AP-XPS before and after annealing in H_2 at 200 °C.

The difference in coordination environment of Rh_1 between Rh_1Co_3/CoO and Rh_1O_n/CoO results in a distinct difference in catalytic performance. Figure 5e,f present the catalytic performances of Rh_1Co_3/CoO and Rh_1O_n/CoO measured under kinetics-control regime. Rh_1O_n/CoO is not active at a temperature of 150 °C and lower. But Rh_1Co_3/CoO is active at 110 °C. In addition, Rh_1O_n/CoO exhibits low selectivity to N_2 production in the temperature range of 150–200 °C. But Rh_1Co_3/CoO exhibits a selectivity of 100% for the reduction of NO to N_2 in this temperature range. The distinct difference between Rh_1O_n/CoO and Rh_1Co_3/CoO in their catalytic performances results from two factors. One is the difference in geometry; the Rh–O–Co of Rh_1O_n/CoO is different from a bimetallic site of Rh_1Co_3/CoO. The existence of a Co–Rh_1–Co on Rh_1Co_3/CoO allows for a strong bonding of two NO molecules (see the following DFT calculations) and thus readily activate NO

molecules compared with Rh_1O_n/CoO. Thus, catalyst of singly dispersed bimetallic sites Rh_1Co_3 is different from the singly dispersed Rh_1 atoms that solely bond to oxygen atoms of the oxide support[22–24].

Location of Rh atoms on CoO. To understand the catalytic mechanism of NO reduction with CO on singly dispersed Rh_1Co_3 anchored on cobalt monoxide, computational modelling of the adsorption, activation and reaction pathway using periodic density functional theory (DFT) was performed. DFT calculations were done for interpretation of the binding environment of Rh atoms (Fig. 6). A Rh atom could anchor to the original position of a missed oxygen (the location of an oxygen vacancy) of CoO in Fig. 6a and thus bond to cobalt atoms; alternatively, it could replace a Co atom of CoO therefore bond to oxygen atoms (Fig. 6c). As shown in Fig. 6a, DFT calculations show that the energy change for filling an oxygen vacancy with a Rh atom is − 5.39 eV, while the energy change for the replacement of a Co atom with a Rh atom on surface is − 3.86 eV. Obviously, filling an oxygen vacancy of CoO with a guest Rh atom is energetically favourable than replacing a Co atom of the surface with a guest Rh atom. This is consistent with the *in situ* measurements of EXAFS of the catalyst in 5% H_2 at 300 °C showing that Rh atoms bond with Co atoms (Fig. 4a and Table 1). Supplementary Fig. 5b is the optimized structure in which the guest Rh atom fills an oxygen vacancy and thus bonds with three cobalt atoms and one oxygen atom.

Optimization of Rh_1Co_3 structural model. In rock-salt CoO crystal, each Co^{2+} is coordinated by six O^{2-} ions in an octahedral crystal field with Co–O distance of 2.13 Å. The (011) surface of CoO with oxygen vacancies can be viewed as an assembled –O–Co–□–Co–O–Co– chain (Supplementary Fig. 5a). When a Rh atom substitutes an oxygen atom on the CoO surface, the Rh_1 atom is not only relocated by 1.13 Å above the vacancy centre (the original oxygen vacancy □, marked with a small light blue ball in Supplementary Fig. 5a), but also moved closer to an oxygen atom shown as a red ball (Supplementary Fig. 5b) in the neighbouring chain with a Rh_1–O distance of 2.04 Å, which is close to a Co–O single bond estimated as 1.9 Å. As a result, the Rh_1 atom only bonds with one neighbouring O atom, while other O atoms are far from the Rh_1 atom by more than 3.3 Å away. In addition, around a Rh_1 atom, there are three Co atoms Co(3), Co(5), Co(7) marked with stars with a Rh–Co distance averagely 2.54 Å in Supplementary Fig. 5b. However, other three cobalt atoms, Co(2), Co(4) and Co(6) around the Rh_1 atom are far from the Rh_1 at a distance of Rh_1–Co(2) at 3.15 Å, Rh_1–Co(4) at 2.81 Å and Rh_1–Co(6) at 3.15 Å. Therefore, the local coordination shell of Rh_1 atom is referred as Rh_1Co_3; the three Co atoms directly coordinating to Rh_1 of Rh_1Co_3 are Co(3), Co(5) and Co(7). This optimized geometry model will be used in all the following calculations.

Adsorption geometry of NO and CO on Rh_1Co_3/CoO. As both the surface Rh and Co atoms can adsorb NO and CO, the preferred adsorption models of NO and CO (Supplementary Fig. 5c–j) were investigated through DFT calculations. Consistent with the orbital interaction analysis, the NO and CO interact with metal atoms through N- and C-side, respectively. By optimizing the adsorption geometries of NO and CO on various sites with different end-on and bridging binding configurations, the adsorption modes and energies of CO and NO on the surface of a Rh_1Co_3/CoO catalyst were evaluated in the DFT calculations. It is found that adsorption of one NO molecule (Supplementary Fig. 5c) on Rh_1 atom is slightly more favourable than that of one
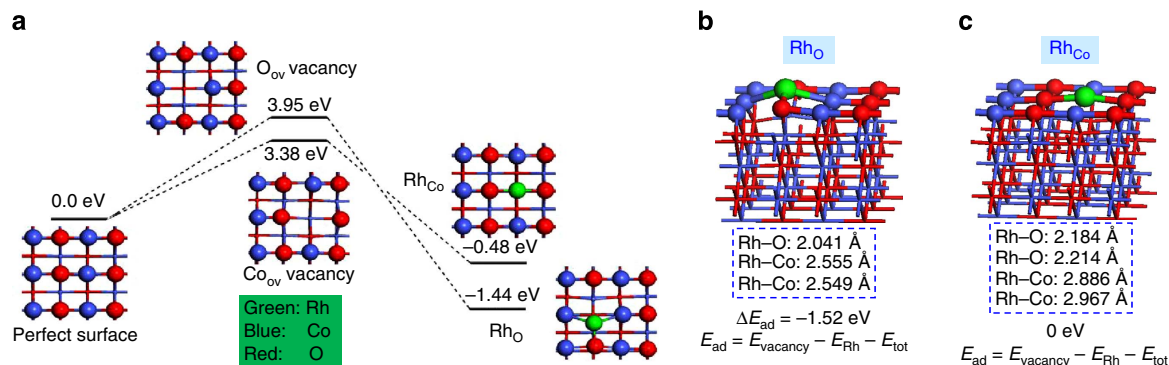
Figure 6 | Computational studies for understanding the site for anchoring a guest atom, Rh. (**a**) Evolution of energy of a surface defect (either O vacancy, O_{vac} or Co vacancy, Co_{vac}) while it is filled with a Rh atom. (**b**) Optimized structure upon filling Rh to oxygen vacancy (Rh_O); in this case the anchored Rh atom bonds with three cobalt atoms and thus a Rh_1Co_3 bimetallic site is formed. (**c**) Optimized structure upon replacing a cobalt atom with a Rh atom (Rh_{Co}); in this case the anchored Rh atom bonds with four oxygen atoms but not with any cobalt atoms; thus it does not form a Rh_1Co_3 bimetallic site if Rh replaces a Co atom.
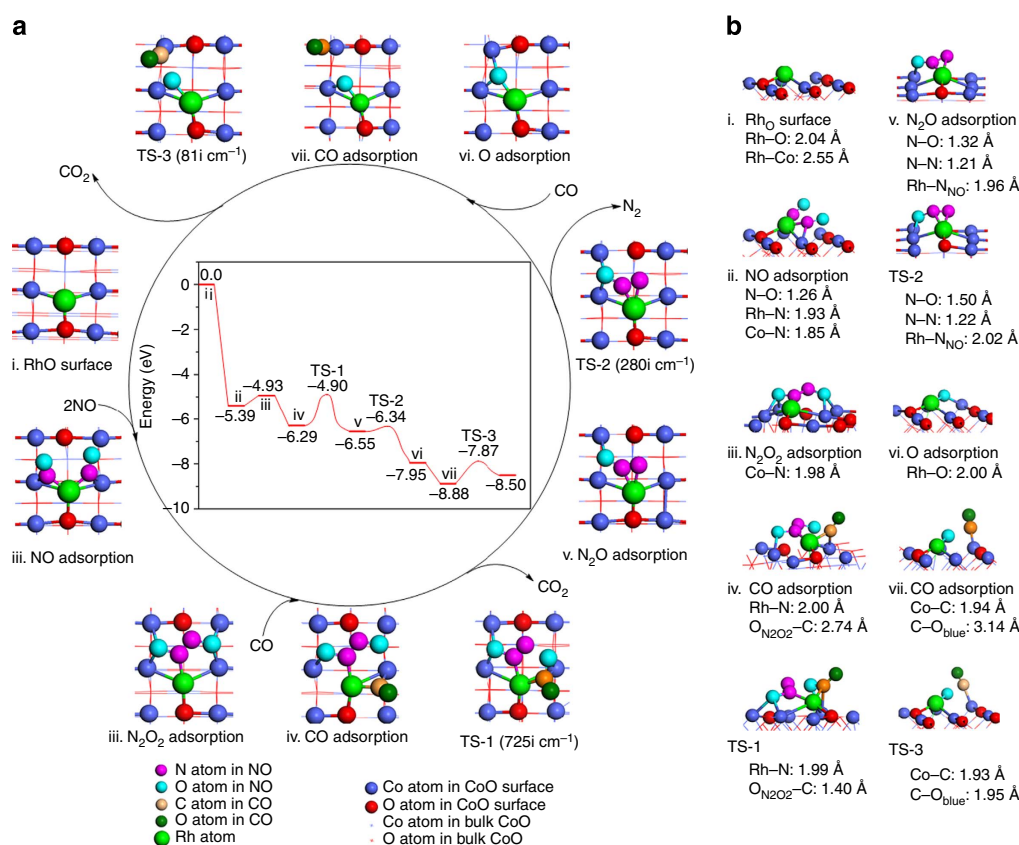
Figure 7 | Reaction pathway. Reaction pathway for reduction of NO with CO on the singly dispersed Rh_1Co_3 supported on CoO proposed from DFT calculations. (**a**) Reaction pathway and energy profile. (**b**) Calculated structural parameters of intermediates and transition states in the pathway.

CO molecule (Supplementary Fig. 5d). Because the singly dispersed Rh atom is not saturated in its coordination shell, co-adsorption is in fact more stable than mono-adsorption. Among all the possible co-adsorption models (Supplementary Fig. 5e–j), two NO molecules co-adsorbed on the Co–Rh_1–Co of Rh_1Co_3 is most stable (Supplementary Fig. 5e). Thus, Rh_1Co_3 adsorbing two NO molecules was used to simulate the reaction pathways and search transition states in the following catalysis studies. Similar to the results for Rh_1Co_3/CoO(011), DFT calculations of the adsorption energies of NO, NO + NO, CO + CO or

CO + NO on Rh_1Co_3/CoO(001) (Supplementary Fig. 6) show that co-adsorption of two NO molecules on Co–Rh_1–Co of Rh_1Co_3/CoO are the strongest adsorption as well.

Reaction pathway. The reaction pathway was calculated for the reduction of NO with CO on a singly dispersed Rh_1Co_3 bimetallic site anchored on CoO (Fig. 7). Briefly, the O_{vac} is filled by a single Rh atom to form a singly dispersed bimetallic site Rh_1Co_3 (step i), which can adsorb two NO molecules on the Co–Rh_1–Co atoms of

Table 2 | Process energies and activation barriers.

Reaction pathway	ΔE (eV)	E_a (eV)
1) $2NO \rightarrow 2NO^*$	-5.39	—
2) $2NO \rightarrow N_2O_2^*$	-4.93	—
3) $CO \rightarrow CO^*$	-0.71	—
4) $N_2O_2^* + CO^* \rightarrow N_2O^* + CO_2$	—	1.39
5) $N_2O^* \rightarrow N_2^* + O^*$	-1.70	0.21
6) $CO \rightarrow CO^*$	-1.07	—
7) $CO^* + O^* \rightarrow CO_2^*$	0.38	1.01

Calculated process energies (ΔE) and activation barriers (Ea) for these elementary steps in the reduction of NO with CO on Rh_1Co_3/CoO in the pathway of Fig. 7. Note: (1) The process energy ΔE is defined as the energy difference between the final state and the initial state. (2) Activation barrier Ea is defined as the difference between the energy of the transition state and the energy of its corresponding initial state.

a Rh_1Co_3 site (step ii); two NO molecules couple on $Co–Rh_1–Co$ to form a N_2O_2 intermediate (step iii) to facilitate the formation of intermediate N_2O; meanwhile one CO molecule can adsorb on the Co atom neighbouring to Rh_1Co_3 (step iv).

The first CO_2 molecule is released after the adsorbed CO molecule couples with one O atom of N_2O_2 adsorbed on the $Co–Rh_1–Co$ site (**TS-1**). This coupling yields a CO_2 molecule and forms an intermediate N_2O remaining on the surface (step v). It is noted that the N–O bond in the intermediate N_2O stretches to form a transition state with a small barrier of 0.21 eV (**TS-2**), which leads to a ready cleavage of N–O bond of the intermediate N_2O and then releases a N_2 molecule and leaves an O atom on Rh_1 (step vi). By adsorbing a second CO on a nearby Co atom (step vii) and then coupling to the left oxygen atoms on the Rh_1 atom, a second CO_2 molecule is released from the surface; thus a catalytic cycle is finished. In this catalytic cycle, the catalyst releases two CO_2 molecules and one N_2 molecule and then recovers its original surface structure (step i in Fig. 7). The inset of Fig. 7a presents the calculated energy profile with the partially reduced system as the reference for the energies in eV. Figure 7b lists the calculated structural parameters of intermediates and transition states of this pathway.

In this reaction pathway, the Rh_1Co_3 site plays a crucial role in the high activity and selectivity in reducing NO with CO. The local coordination environment of the bimetallic site Rh_1Co_3 helps to activate the two NO molecules on $Co–Rh_1–Co$ of Rh_1Co_3 through co-adsorption and coupling. The catalytic elementary steps, evolution of energies and activation barriers are listed in Table 2. Especially noteworthy is the extremely low activation barrier of N_2O decomposition (0.21 eV) to a N_2 molecule on the Rh_1Co_3/CoO catalyst. Given the high reaction temperature, this step is virtually barrierless in terms of Gibbs free energies. Thus, these calculation results are quite consistent with the fact that the catalyst of Rh_1Co_3 bimetallic sites is active at a temperature as low as 110 °C with a selectivity of 100% for production of N_2.

Other than the formation of a N_2 molecule through breaking N–O bond of the intermediate N_2O (v of Fig. 7), we further considered other pathways. For instance, N atom formed through dissociation of one of the two NO molecules (i of Supplementary Fig. 7) could couple with a N atom of another NO molecule that bonds to an oxygen vacancy through the oxygen atom of NO (ii of Supplementary Fig. 7); this coupling weakens N–O bond of the adsorbed NO molecule and thus forms a N_2 species strongly adsorbed on the Rh atom with a quite high adsorption energy (iv of Supplementary Fig. 7). The barrier of the transition state (iii of Supplementary Fig. 7) to form N_2 molecule is 0.5 eV. However, the binding energy of N_2 molecule on Rh atom is quite large (iv of Supplementary Fig. 7), which makes this pathway less favourable.

Discussion
To understand the difference in binding of NO molecules on isolated sites Rh_1Co_3 supported on CoO and surface of a Rh–Co bimetallic nanoparticle supported on CoO, structural models of Rh_1Co_3/CoO with one adsorbed NO molecule (Supplementary Fig. 8a) and Rh–Co bimetallic nanoparticle/CoO with one adsorbed NO molecule (Supplementary Fig. 8b) were built. DFT calculations show that adsorption of a NO molecule on Rh atom of Rh_1Co_3 is definitely stronger than that on a zero-valent Rh(0) atom of a Rh–Co bimetallic nanoparticle (Supplementary Table 3). Consistent with this difference, the calculated $N \cdots Rh$ distance of Rh_1Co_3/CoO is ~ 0.03 Å smaller in contrast to that of Rh–Co bimetallic nanoparticle/CoO. These differences suggest that the Rh_1Co_3/CoO catalyst can readily activate NO compared with Rh–Co bimetallic nanoparticle/CoO.

The computed electron density difference maps of the two different fragments on Rh_1Co_3/CoO and Rh–Co bimetallic nanoparticle/CoO are shown in Supplementary Fig. 8c and d, respectively. In these plots (Supplementary Fig. 8c and d), a decrease in electron density is shown in blue, electron enrichment indicated in red; white region indicates little change in electron density. The more red colour between N and Rh in Rh_1Co_3/CoO (Supplementary Fig. 8c) than the one in the Rh–Co bimetallic nanoparticle supported on CoO (Supplementary Fig. 8d) shows that the Rh–N bond on Rh_1Co_3/CoO is stronger than that on Rh–Co nanoparticles supported on CoO. Thus the charge transfer from NO to Rh atoms of Rh_1Co_3/CoO is larger than that on Rh–Co bimetallic nanoparticle/CoO. The calculated Bader charges (Supplementary Table 4) revealed that the Rh_1 single atom of Rh_1Co_3/CoO carries positive charge upon adsorption of NO while the Rh atom in Rh–Co alloy NP/CoO carries negative charge upon NO adsorption. The positive charge on Rh_1 of a singly dispersed Rh_1Co_3 site allows more electron transfer from NO, which enhances the Rh–N bond and thus largely weakens the N–O bond of NO molecule on Rh_1Co_3.

The spin-polarized projected density of states (PDOS) of the $4d$ states of Rh atom and the N-$2p$ and O-$2p$ orbitals of adsorbed NO on Rh_1Co_3/CoO and Rh–Co bimetallic nanoparticle/CoO are shown in Supplementary Fig. 8e and f, respectively. The spin-polarized projected density of states show that below the Fermi level (E_F) Rh $4d$ states in Rh_1Co_3/CoO catalyst are more localized than the Rh $4d$ states in Rh–Co bimetallic nanoparticle/CoO. In addition, Rh $4d$ states in Rh_1Co_3/CoO (Supplementary Fig. 8e) are mixed better with N $2p$ and O $2p$ states than Rh $4d$ states in Rh–Co bimetallic nanoparticle/CoO (Supplementary Fig. 8f), indicating a strong interaction between Rh_1 atom of Rh_1Co_3 and the adsorbed NO molecule.

One critical difference between a singly dispersed Rh_1Co_3 site anchored on CoO and a Rh–Co bimetallic nanoparticle supported on CoO is the 100% selectivity for production of N_2 in reduction of NO with CO on Rh_1Co_3 (Fig. 5a). On Rh–Co bimetallic nanoparticle supported on CoO (Fig. 5d), however, selectivity for production of N_2 is only 10%. To understand this difference in catalytic selectivity for production of N_2O on the two surfaces, structural models of Rh_1Co_3/CoO and Rh–Co bimetallic nanoparticle/CoO (Supplementary Fig. 9) were built. The calculated adsorption energies of N_2O for Rh_1Co_3/CoO and Rh–Co bimetallic nanoparticles/CoO are -1.56 and -0.85 eV, respectively. N_2O is the by-product of the reduction of NO with CO; it is also the intermediate for production of N_2 (step 5 in Table 2). A stronger binding of N_2O prevents it from molecular desorption. Thus, the selectivity for the production of N_2O on Rh_1Co_3/CoO is low since the adsorption of N_2O on Rh_1Co_3/CoO is stronger than that on Rh–Co bimetallic nanoparticle/CoO. In addition, as the activation barrier for dissociating N_2O to N_2 and

O on Rh_1Co_3/CoO is only 0.21 eV (**TS**-2 in Fig. 7), N_2O can readily dissociate to N_2 on Rh_1Co_3/CoO at a relatively low temperature. Overall, the stronger binding of N_2O on Rh_1Co_3 site and the rather low activation barrier for dissociation of the intermediate N_2O to N_2 on Rh_1Co_3/CoO, make the reduction of NO to N_2 with a high selectivity at a relatively low temperature in contrast to Rh–Co bimetallic nanoparticles/CoO.

As described in literature[25], the test temperature of engine of a gasoline vehicle is 1,100 °F (593 °C), stability tests by measurements of conversion and selectivity of the catalyst, Rh_1Co_3/CoO were performed. Concerning the real hydrothermal conditions in a three-way catalytic reactor, water vapour was also introduced to the reactor to simulate the exhaust of gasoline engines. As shown in literature[26], typically the composition of water vapour is 20 times of nitric oxide and carbon monoxide. Thus, stability of 10 mg catalyst was tested in a mixture of 12 ml min^{-1} NO, 12 ml min^{-1} CO, 68 ml min^{-1} Ar and H_2O vapour generated from 0.18 ml min^{-1} water were mixed and then introduced to a fixed-bed flow reactor. The molar ratio of $NO:CO:H_2O$ is 1:1:20. The conversion and selectivity of this catalyst remained nearly constant within 168 h.

These studies suggest that the isolation of bimetallic sites on non-metallic supports is a promising approach for developing catalysts, since such centres exhibit cationic states and offer the fewest binding configurations for reactant molecules—distinctly different from bimetallic nanoparticles.

Methods

Preparation of isolated Rh_1Co_3 sites on cobalt oxide. Co_3O_4 nanorods were synthesized with a modified wet chemistry method in literature[27]. To synthesize a catalyst of singly dispersed Rh_1Co_3 sites, Co_3O_4 nanorods were synthesized with a modified wet chemistry method and a following calcination at high temperature[27,28]. Then, species of rhodium precursor were introduced on the crystallized Co_3O_4 nanorods through a deposition–precipitation with a mass ratio of Rh to Co_3O_4 of 0.25 wt%.

$Rh(NO_3)_3$ (Sigma-Aldrich, ~36% Rh basis; 0.28 g) was dissolved in water via a 50 ml volumetric flask. Co_3O_4 nanorods (0.80 g) was dispersed in 50.0 g deionized water with strong agitation to make a homogeneous black suspension. The prepared $Rh(NO_3)_3$ aqueous solution was added by micropipette to the suspension of dispersed Co_3O_4 nanorods. Vigorous stirring for 1 h is necessary to make sure a homogeneous distribution and preliminary natural adsorption of Rh^{3+} on the surface of Co_3O_4 nanorods. The pH was then gradually adjusted to 9.0 by ammonium hydroxide solution monitored with a pH meter. After that, the solution was stirred vigorously for another 12 h to reach an equilibrium for a thorough, homogeneous adsorption of Rh^{3+} ions and followed by washing with deionized water and centrifuged. The catalyst precursor was dried in vacuum at 70 °C for at least 12 h. Then it was oxidized and reduced at an appropriate temperature so that the singly dispersed bimetallic site Rh_1Co_3 can be prepared.

Synthesis of Rh–Co bimetallic nanoparticles supported on CoO and Rh–Co alloy nanoparticles/SiO_2 (Rh: 5 wt%) was achieved by aqueous impregnation of Rh and Co precursors to SiO_2 NPs or Co_3O_4 nanorods. $Rh(NO_3)_3$·xH_2O (Sigma-Aldrich, ~36% Rh basis) and $Co(NO_3)_3$·$6H_2O$ (Sigma-Aldrich, ≥98%) were used as precursors of Rh and Co, respectively. The total weight per cent of Rh and Co is 5 wt% while keeping the atomic ratios of the loaded Rh and Co identical. $Rh(NO_3)_3$·xH_2O and $Co(NO_3)_3$·$6H_2O$ were dissolved in deionized water to make a clear solution. SiO_2 (0.5 g) or Co_3O_4 nanorods (0.5 g) were immersed into the solution. The water was gradually evaporated at 60 °C with vigorous stirring and the catalyst was then dried in vacuum at 60 °C for 12 h, followed by calcination in 5% O_2 at 150 °C for 3 h. Before catalytic measurement, the catalyst was pretreated at 300 °C in 5% H_2.

Rh_1O_n/CoO was synthesized by introduction of Rh cations to well-prepared CoO by deposition–precipitation with a following annealing in N_2 and then a reduction at 200 °C in 5% H_2 for 1 h.

In situ studies using ambient pressure X-ray photoelectron spectroscopy. In situ studies of surface chemistry of these catalysts were performed on the ambient pressure XPS using monochromated Al Kα in the Tao group[11,29,30]. The binding energy of catalyst samples were calibrated to Au $4f_{7/2}$ at 84.0 eV and Ag $3d_{5/2}$ at 368.3 eV (ref. 11). In the AP-XPS studies, one or more reactant gases were introduced into a reactor. A sample is inserted and placed at the cross point of Rowland cycle of the monochromator and trajectory line of photoelectrons in lens of differentially pumped energy analyser. A distance between sample surface and the aperture of pre-lens of the differential pumping stage remains at ~0.5 mm,

which is shorter than the mean free paths of photoelectrons travelling in a gaseous environment of 5 Torr.

Measurements of catalytic performance for reduction of NO with CO. Reduction of NO with CO on catalysts is performed in a fixed-bed flow reactor. Gas computations and flow rates were marked in captions of figures. Details of catalytic measurement using our fixed-bed flow reactor can be found in our previous publications[9,10].

***In situ* studies using XANES and EXAFS.** In situ X-ray absorption spectroscopy (XANES) measurements were performed at the beamline X18B at the National Synchrotron Light Source, Brookhaven National Laboratory. The samples were made by pressing the powders into circular pellets using hydraulic press and transferred onto a sample holder of a Nashner–Adler in situ cell[31].

The data in the XANES region of the absorption coefficient were analysed by applying the same procedure for pre-edge line fitting, post-edge curve fitting and edge-step normalization to all the data. The XANES and extended X-ray absorption fine structure (EXAFS) data processing and analysis were performed using the IFEFFIT package[32]. The EXAFS data modelling and analysis were performed using standard procedures[32–36].

Computational methods. The calculations were performed with the Vienna Ab-initio Simulation Package (VASP version 5.2). Both (011) and (001) surfaces of cobalt monoxide were represented by a periodic slab model constructed using bulk cell dimensions: $a = b = c = 4.2667$ Å (ref. 37). Only calculation results of (011) surface were described in the main text. Since CoO is antiferromagnetic and has atomic moment on cobalt atoms, the primitive cubic unit cell of CoO was used to build the surface slab, which was previously proved to be the most energetically stable configuration for CoO[38]. The repeated slabs were separated from their neighbouring images by a 12 Å-width vacuum in the direction perpendicular to the surface. Considering the usually very large relaxations of the CoO surfaces, a slab containing five layers of 60 atoms was chosen. The three top-layer slabs of the surface were allowed to relax while the other layers beneath the surface were frozen during the geometry optimization (Supplementary Fig. 10).

The core and valence electrons were represented by the projector-augmented wave method and plane-wave basis functions with a kinetic energy cut-off of 400 eV. Inasmuch as Rh has non-negligible relativistic effects, the mass–velocity and Darwin relativistic effects were included through the projector-augmented wave potentials. The generalized gradient approximation with the Perdew–Burke–Ernzerhof exchange-correlation functional was used in the calculations. A Monkhorst–Pack grid of size of $2 \times 2 \times 1$ was used to sample the surface Brillouin zone. Ground-state atomic geometries were obtained by minimizing the forces on the atoms to <0.02 eV Å^{-1}. Because of the strong d-electron correlation effects for Co, the calculations were carried out with the DFT + U method. The parameters were set at $U = 4$ eV and $J = 1$ eV according to previous reports[39] and our investigation (Supplementary Tables 5, 6). The transition states were obtained by relaxing the force <0.02 eV Å^{-1} by using the dimer method[40].

References

1. Somorjai, G. A. L. Y. M. *Introduction to Surface Chemistry and Catalysis*. 2nd Edition (Wiley, 2010).
2. Ertl, G., Knözinger, H., Schuth, F. & Weitkamp, J. *Handbook of Heterogeneous Catalysis* (Wiley-VCH, 2008).
3. Guo, X. *et al.* Direct, nonoxidative conversion of methane to ethylene, aromatics, and hydrogen. *Science* **344**, 616–619 (2014).
4. Chen, M. S., Kumar, D., Yi, C. W. & Goodman, D. W. The promotional effect of gold in catalysis by palladium-gold. *Science* **310**, 291–293 (2005).
5. Kyriakou, G. *et al.* Isolated metal atom geometries as a strategy for selective heterogeneous hydrogenations. *Science* **335**, 1209–1212 (2012).
6. Zhu, Y. *et al.* Catalytic conversion of carbon dioxide to methane on ruthenium-cobalt bimetallic nanocatalysts and correlation between surface chemistry of catalysts under reaction conditions and catalytic performances. *ACS Catal.* **2**, 2403–2408 (2012).
7. Chen, J., Wu, X. F. & Selloni, A. Electronic structure and bonding properties of cobalt oxide in the spinel structure. *Phys. Rev. B* **83**, 245204 (2011).
8. Xie, X. W., Li, Y., Liu, Z. Q., Haruta, M. & Shen, W. J. Low-temperature oxidation of CO catalysed by Co_3O_4 nanorods. *Nature* **458**, 746–749 (2009).
9. Zhang, S. *et al.* Restructuring transition metal oxide nanorods for 100% selectivity in reduction of nitric oxide with carbon monoxide. *Nano Lett.* **13**, 3310–3314 (2013).
10. Zhang, S. *et al.* WGS catalysis and in situ studies of CoO_{1-x}, $PtCon/Co_3O_4$, and Pt_nCo_m/CoO_{1-x} nanorod catalysts. *J. Am. Chem. Soc.* **135**, 8283–8293 (2013).
11. Tao, F. Design of an in-house ambient pressure AP-XPS using a bench-top X-ray source and the surface chemistry of ceria under reaction conditions. *Chem. Commun.* **48**, 3812–3814 (2012).
12. Moulder, J. F. S., Sobol, W. F. & Bomben, P. E. K. D. *Handbook of X-ray Photoelectron Spectroscopy* (Perkin-Elmer Corporation, 1992).

13. Yang, J. C., Small, M. W., Grieshaber, R. V. & Nuzzo, R. G. Recent developments and applications of electron microscopy to heterogeneous catalysis. *Chem. Soc. Rev.* **41,** 8179–8194 (2012).

14. Chuang, T. J., Brundle, C. R. & Rice, D. W. Interpretation of X-ray photoemission spectra of cobalt oxides and cobalt oxide surfaces. *Surf. Sci.* **59,** 413–429 (1976).

15. Petitto, S. C., Marsh, E. M., Carson, G. A. & Langell, M. A. Cobalt oxide surface chemistry: the interaction of CoO(100), Co$_3$O$_4$(110) and Co$_3$O$_4$(111) with oxygen and water. *J. Mol. Catal. A Chem.* **281,** 49–58 (2008).

16. Renzas, J. R., Zhang, Y. W., Huang, W. Y. & Somorjai, G. A. Rhodium nanoparticle shape dependence in the reduction of NO by CO. *Catal. Lett.* **132,** 317–322 (2009).

17. Gao, F., Wang, Y. & Goodman, D. W. CO/NO and CO/NO/O$_{-2}$ reactions over a Au-Pd single crystal catalyst. *J. Catal.* **268,** 115–121 (2009).

18. Lambrou, P. S. & Efstathiou, A. M. The effects of Fe on the oxygen storage and release properties of model Pd-Rh/CeO$_2$-Al$_2$O$_3$ three-way catalyst. *J. Catal.* **240,** 182–193 (2006).

19. Maillet, T., Barbier-Jr, J., Gelin, P., Praliaud, H. & Duprez, D. Effects of pretreatments on the surface composition of alumina-supported Pd-Rh catalysts. *J. Catal.* **202,** 367–378 (2001).

20. Rider, K. B., Hwang, K. S., Salmeron, M. & Somorjai, G. A. High-pressure (1 Torr) scanning tunneling microscopy (STM) study of the coadsorption and exchange of CO and NO on the Rh(111) crystal face. *J. Am. Chem. Soc.* **124,** 5588–5593 (2002).

21. Herman, G. S., Peden, C. H. F., Schmieg, S. J. & Belton, D. N. A comparison of the NO-CO reaction over Rh(100), Rh(110) and Rh(111). *Catal. Lett.* **62,** 131–138 (1999).

22. Yang, X.-F. *et al.* Single-atom catalysts: a new frontier in heterogeneous catalysis. *Acc. Chem. Res.* **46,** 1740–1748 (2013).

23. Qiao, B. *et al.* Single-atom catalysis of CO oxidation using Pt$_{-1}$/FeO$_x$. *Nat. Chem.* **3,** 634–641 (2011).

24. Lin, J. *et al.* Remarkable performance of Ir$_1$/FeO$_x$ single-atom catalyst in water gas shift reaction. *J. Am. Chem. Soc.* **135,** 15314–15317 (2013).

25. Harrison, R. T. *Catalytic converter exhaust system temperature tests.* (U.S. Department of Agriculture, Equipment Development Center (1977).

26. Srinivasan, A. & Depcik, C. Review of chemical reactions in the NO reduction by CO on rhodium/alumina catalysts. *Catal. Rev. Sci. Eng.* **52,** 462–493 (2010).

27. Xie, X. W. *et al.* Synthesis of nanorod-shaped cobalt hydroxycarbonate and oxide with the mediation of ethylene glycol. *J. Phys. Chem. C* **114,** 2116–2123 (2010).

28. Wang, L. *et al.* Catalysis and *In Situ* studies of Rh$_{-1}$/Co$_3$O$_4$ nanorods in reduction of NO with H$_{-2}$. *ACS Catal.* **3,** 1011–1019 (2013).

29. Shan, J. J. *et al.* Catalytic performance and *in situ* surface chemistry of pure alpha-MnO$_2$ nanorods in selective reduction of NO and N$_2$O with CO. *J. Phys. Chem. C* **117,** 8329–8335 (2013).

30. Tao, F. *et al.* Understanding complete oxidation of methane on spinel oxides at molecular level. *Nat. Commun.* **6,** 7798 doi:10.1038/ncomms8798 (2015).

31. Nashner, M. S., Frenkel, A. I., Adler, D. L., Shapley, J. R. & Nuzzo, R. G. Structural characterization of carbon-supported platinum-ruthenium nanoparticles from the molecular cluster precursor PtRu$_5$C(CO)$_{(16)}$. *J. Am. Chem. Soc.* **119,** 7760–7771 (1997).

32. Newville, M. IFEFFIT: interactive XAFS analysis and FEFF fitting. *J. Synchrotron Rad.* **8,** 322 (2001).

33. Frenkel, A. I., Hills, C. W. & Nuzzo, R. G. A view from the inside: complexity in the atomic scale ordering of supported metal nanoparticles. *J. Phys. Chem. B* **105,** 12689–12703 (2001).

34. Frenkel, A. Solving the 3D structure of metal nanoparticles. *Z Kristallogr.* **222,** 605–611 (2007).

35. Frenkel, A. I. Applications of extended X-ray absorption fine-structure spectroscopy to studies of bimetallic nanoparticle catalysts. *Chem. Soc. Rev.* **41,** 8163–8178 (2012).

36. Frenkel, A. I., Yevick, A., Cooper, C. & Vasic, R. Modeling the structure and composition of nanoparticles by extended X-ray absorption fine-structure spectroscopy. *Annu. Rev. Anal. Chem.* **4,** 23–39 (2011).

37. Henrich, V. E. & Cox, P. A. *The Surface Science of Metal Oxides* (Cambridge University Press, 1996).

38. Wyckoff, R. W. G. *Crystal Structure* 2nd edition (Interscience Publishers, 1965).

39. Wang, L., Maxisch, T. & Ceder, G. Oxidation energies of transition metal oxides within the GGA + U framework. *Phys. Rev. B* **73,** 195107 (2006).

40. Henkelman, G. & Jonsson, H. A dimer method for finding saddle points on high dimensional potential surfaces using only first derivatives. *J. Chem. Phys.* **111,** 7010–7022 (1999).

Acknowledgements

Author contributions

F.T. launched the project of catalysis on singly dispersed bimetallic sites of his NSF Career Award, designed the synthesis, catalysis and *in situ* characterizations of singly dispersed bimetallic sites, analysed the experimental results and wrote this paper. J.L. designed the theoretical studies and wrote the computational part. S.Z. performed majority of the experiments. L.N. interpretation of the experimental results and participated in the writing. J.-X.L. performed the theoretical calculations. J.L (Liu) performed HAADF-STEM. S.Z and A.P. performed the EXAFS experiments. A.I.F. analysed the EXAFS data. J.S. and W.H. collected some of the AP-XPS data.

Additional information